PCCP

PAPER

Cite this: *Phys. Chem. Chem. Phys.*, 2017, **19**, 7176

Anticipating hyperthermic efficiency of magnetic colloids using a semi-empirical model: a tool to help medical decisions†

M. B. Fernández van Raap,*[a] D. F. Coral,[a] S. Yu,[b] G. A. Muñoz,[a] F. H. Sánchez[a] and A. Roig[b]

Received 24th November 2016,
Accepted 7th February 2017

DOI: 10.1039/c6cp08059f

rsc.li/pccp

Magnetic hyperthermia, a modality that uses radio frequency heating assisted with single-domain magnetic nanoparticles, is becoming established as a powerful oncological therapy. Much improvement in nanomaterials development, to enhance their heating efficiency by tuning the magnetic colloidal properties, has been achieved. However, methodological standardization to accurately and univocally determine the colloidal properties required to numerically reproduce a specific heating efficiency using analytical expressions still holds. Thus, anticipating the hyperthermic performances of magnetic colloids entails high complexity due to polydispersity, aggregation and dipolar interactions always present in real materials to a greater or lesser degree. Here, by numerically simulating the experimental results and using real biomedical aqueous colloids, we analyse and compare several approaches to reproduce experimental specific absorption rate values. Then, we show that the relaxation time, determined using a representative mean activation energy consistently derived from four independent experiments accurately reproduces experimental heating efficiencies. Moreover, the so-derived relaxation time can be used to extrapolate the heating performance of the magnetic nanoparticles to the other field conditions within the framework of the linear response theory. We thus present a practical tool that may truly aid the design of medical decisions.

1. Introduction

Magnetic hyperthermia (MH) is an oncological therapy[1] under clinical trial that is achieved by subjecting biocompatible magnetic nanoparticles to external radio frequency fields of 100 kHz and 15 kA m^{-1}. Besides that, the synergistic potential of MH combined with other clinically approved treatments like chemo,[2] radio[1] and photodynamic[3] therapies is under scrutiny. Iron oxide nanoparticles (IONPs), magnetite (Fe_3O_4) or maghemite (γ-Fe_2O_3), coated with polyprotic acids like dimercaptosuccinic[4] or citric acids,[5] polysaccharides like dextran[6,7] and aminosilane hydrophilic[8] molecules and well dispersed in water at physiological pH are widely accepted as the most biocompatible materials for MH treatments. For clinical trials of MH associated with radiotherapy, IONPs coated with aminosilane were used,[1] and Jordan showed that aminosilane coated IONPs displayed better efficiency compared with carboxidextran coated particles.[8]

By increasing the temperature, hyperthermia causes living cell death when the temperature reaches values in the range from 42 to 46 °C. This abnormally high temperature alters the function of many structural and enzymatic proteins within cells, which in turn alters cell growth and differentiation and can induce apoptosis. Among the various hyperthermic modalities, MH provides spatial selectivity avoiding normal tissue damage. A comparison of the various hyperthermic therapeutic modalities in terms of clinical results, side effects, and limitations can be found in P. Moroz *et al.*'s review.[9] A more recent review on the status of MH in clinical trials can be found elsewhere.[10]

Under the effect of an alternating current (a.c.) magnetic field in the radio frequency range, an assembly of single-domain (SD) magnetic nanoparticles (MNPs) absorbs energy from the field achieving a magnetization which lags in phase relative to the excitation wave.[11] The energy absorbed by the nanoparticles is then released to the environment. When the MNPs located in tumour tissue are subjected to the a.c. field and release enough energy to increase the temperature up to therapeutic values (42–45 °C), the apoptosis of tumour cancer cells is induced.[12] Increasing the temperature above 45 °C and up to 50 °C results

[a] *Instituto de Física La Plata (IFLP-CONICET), Departamento de Física, Facultad de Ciencias Exactas, Universidad Nacional de La Plata (UNLP), c.c. 67, 1900 La Plata, Argentina. E-mail: raap@fisica.unlp.edu.ar; Fax: +54 221 4236335; Tel: +54 221 4246062 ext. 257*

[b] *Institut de Ciència de Materials de Barcelona (ICMAB-CSIC), Campus UAB, 08193 Bellaterra, Catalonia, Spain*

† Electronic supplementary information (ESI) available. See DOI: 10.1039/c6cp08059f

in cell/tumour ablation. The results presented here are useful for both hyperthermia and ablation. A parameter often used to characterize the MNP efficiency at a given field is the specific absorption rate (SAR), keeping in mind that this parameter depends on field conditions.

In addition, RF heating has also been proposed in drug delivery applications. Nanoparticles are designed to release their drug payload in response to an external stimulus like light, ultrasound, heat and medium acidity.[13] Iron oxide nanoparticles embedded in poly(lactic-*co*-glycolic acid) and loaded with paclitaxel have been recently reported where magnetic hyperthermia was used to trigger drug release by Néel relaxation.[14] Interestingly the authors were able to correlate the SAR values of the investigated systems with the particle size obtained from the ^{1}H nuclear magnetic resonance dispersion profiles and argued that proton nuclear magnetic resonance could be used to predict the SAR of new systems.

Regarding medical aspects, Hilger[15] has stressed in her recent *in vivo* review that besides the huge advantage coming from the fact that heating is generated within the tumour and not from outside the body, the optimal dose of MNPs and their intratumoral distribution are key factors determining the therapeutic outcome. In addition, dosage relies on the nanoparticle properties and on administration routes. Earlier it was recognized that the optimization of the nanoparticle properties will allow the dose to be reduced and the use of moderate a.c. fields in terms of field frequency, f, and field amplitude, H_0 (within the biomedically safe range of a.c. applications, *i.e.* $f{\cdot}H_0$ below 4.85×10^8 A m^{-1} s^{-1}) to achieve the desired effect. To this end, it is essential to enhance the heating efficiency of iron oxide nanoparticles,[16] reduce early clearance from the body and minimize non-specific cell interactions, thus minimizing side effects. This situation has led to the improvement of chemical synthesis and coating protocols for producing IONPs sterically or electrostatically stabilized in a physiological medium and to provide specificity for intravenous applications. These protocols include co-precipitation of iron salts,[17,18] thermal decomposition of a metal complex,[19,20] hydrothermal polyol processes[21] and laser target evaporation[22] among others. More recently, these methods have been enlarged by improving heating during chemical reactions with the assistance of microwaves (MWs).[23,54] MW-assisted routes display the advantages of producing particles in high yields within a few minutes and that the particles are straightforwardly stabilized as aqueous colloidal dispersions at physiological pH. This avoids the ligand exchange step needed in a conventional thermal decomposition route which often results in partial aggregation of the particles. Using a microwave-based method, the synthesis of water stable citric-acid coated multi-core iron oxide nanoparticles suitable for magnetic heating has been reported.[24]

Besides magnetosomes, which may not be suitable for biomedical applications unless prepared under specific conditions,[25] the largest specific heating efficiencies have been reported for crystalline magnetite nanoparticles with core sizes between 20 and 30 nm, in the transition zone between the single magnetic domain and the multidomain,[26] where values as large as 300 W g_{Fe}^{-1} for 22 nm at 77 kHz and 40 kA m^{-1} were achieved. Spherical clusters (60 nm size) of carboxymethyl dextran coated iron oxide nanoparticles of 18 nm size dissipate 720 W g^{-1} when excited at 10 kA m^{-1} and 410 kHz[18] and nanoflower like assemblies[21] dissipate 1175 W g^{-1} when excited at 21.5 kA m^{-1} and 700 kHz. Cubic shape particles also display large SAR values due to the shape anisotropy contribution.[27] SAR values of several nanoparticles under excitation frequencies larger than 200 kHz in various environments have also been recently reported.[28] Another way to improve the SAR is by modifying MNP chemical composition, for instance by doping with Zn[46] or Mn to increase magnetization that effectively leads to an increase in the MNP heating efficiency, or by using exchange coupled nanomagnets, combining hard and soft magnetic phases like $CoFe_2O_4$@$MnFe_2O_4$.[29] In all of these studies SAR trends are verified but the measured SAR magnitudes were not theoretically reproduced.

Moreover, nanoparticle aggregation influences heat dissipation, and contradictory results have been reported. A negative influence of aggregation on the SAR has been observed in samples where the aggregates are composed of randomly oriented spherical nanoparticles.[30–32] Materia *et al.*[33] have analyzed the performance of mesoscale assemblies of cubic IONPs to generate controlled aggregates. The authors showed that the hyperthermic performance of these aggregates was lower than that of their counterpart IONPs due to dipolar interactions. On the other hand, it has been proposed that assembling cubic particles in elongated chains (uniaxial anisotropy) is a strategy to increase the MH performance.[27,34] Furthermore, the possibility of controlling heating power by tuning dipolar interactions first led to controversial results indicating that the SAR both increases and decreases with increasing concentration.[20,35–38] We have recently clarified this point by proving experimentally that the power dissipated by an ensemble of monodisperse magnetic nanoparticles becomes a non-extensive property as a direct consequence of the long-range nature of dipolar interactions, *i.e.* specific heat dissipation displays a maximum against concentration.[31] Similarly non-monotonic concentration dependence was shown by Conde-Leboran *et al.*[39] This concentration trend has already been proposed by Landi[40,41] using a random dipolar-field approximation, for the mean first order fluctuating dipolar field contribution averaging to zero, *i.e.* only valid for an ensemble of monodisperse MNPs. Haase *et al.*[42] indicated a negative influence of the dipole–dipole interactions on heating power and a maximum in the heating power per sample volume *vs.* concentration based on the Landau–Lifschitz–Gilbert equation of motion solved with Langevin dynamics for the various spatial distributions of MNP. In spite of these efforts, the only parameters that nowadays can be used to control heating are the field parameters f and H_0 but to this end a way to predict the SAR magnitude of a given colloidal system has to be established. Abenojar *et al.* have recently published a more detailed review including size, shape, chemical composition and dipolar interaction effects on magnetic hyperthermia and more importantly, have introduced a new theranostic modality based on magnetic imaging guided hyperthermia.[43]

In general, a fingerprint of highly dissipating MNP assemblies is a blocking temperature (T_b) close or above room temperature, for an experimental temporal window, typical of d.c. magnetometry. For instance, a progressive shift of T_{bm} (the maximum shown by zero-field-cooled magnetization) from 70 K to temperatures higher than 300 K was observed by Salas *et al.*[44] on highly crystalline, monodisperse, and interactive assemblies of SD-IONPs coated with *meso*-2,3-dimercaptosuccinic acid, when the MNP size increased from 7 to 22 nm (SAR increases from 4.62 to 320 W g_{Fe}^{-1}). Di Corato *et al.*[28] reported T_{bm} going from 135 K to values larger than 320 K for samples going from co-precipitated maghemite nanoparticles ~10 nm in size (135 K), to a 250 nm assembly of the same maghemite nanoparticles in liposomes (165 K), iron oxide/gold dimers of 15 nm size (175 K), iron oxide nanoflowers of 25 nm size (280 K), iron oxide nanocubes of 18 nm size on the edge (300 K) and cobalt ferrite nanoparticles of 10 nm size ($\gg$320 K), together with increasing SAR magnitudes. The blocking temperature increases with the MNP size and the value corresponding to a given size shifts to higher values when the dipolar interaction strength increases.[45] Unfortunately, the T_{bm} of these highly dissipating colloids is above the limit of the available temperature range of standard SQUID and PPMS magnetometry measuring systems.

Although much knowledge has been established, there is still no clear consensus about the specific key features of a colloid needed for predicting its SAR, nor about the analytical expression to semi-empirically reproduce measured SAR values. Exhaustive structural and magnetic characterization of the so-produced colloids has been commonly carried out to derive interrelation between their nanoparticle physical properties and their specific heating efficiency, but these properties are barely used to numerically reproduce the experimental SAR values. Attempts to numerically reproduce measured SAR magnitudes[31,46–50] in general failed because the MNP dispersions present polydispersity, aggregation and dipolar interaction and there is a lack of knowledge about the effect of these properties on the energy barrier and relaxation time. Also discrepancies between characteristic magnitudes derived from different techniques appear. In this sense standardization of the measurement protocols to accurately and univocally determine colloidal properties is still needed. For instance, often there are discrepancies between effective anisotropy constant K_{eff} values derived by d.c. and a.c. magnetometry, and a diverse range of criteria to retrieve this magnitude from raw data and Néel prefactor τ_0 values in a range as wide as 10^{-12} to 10^{-8} s are used. As a result, which physical properties of a given suspension of MNPs must be determined, and how to securely predict the heating efficiency at any pre-set applied field using an analytical expression are still open questions. This is indeed the main goal of this work since it would constitute a practical tool for assisting medical decisions. More precisely, to decide which is the optimal dosage of a given nanoparticle to be intra-tumorally injected considering the tumour volume in order to achieve the desired temperature increase, ΔT, in a time t under excitation of parameters f and H_0.

To this end, we tested the applicability of quasi-static (d.c.) and low frequency a.c. methodologies to derive the activation energy which defines Néel relaxation times, and to numerically reproduce the experimentally measured SAR data. We have analysed five model systems of stable colloidal aqueous suspensions including: citric acid coated γ-Fe_2O_3 nanoparticles produced by a microwave-assisted thermal decomposition method,[53] two different multicore suspensions of chitosan particles holding aggregated Fe_3O_4 nanoparticles or holding well dispersed MNPs prepared by co-precipitation of magnetite followed by chitosan nanoprecipitation on as-formed MNPs[51] and uncoated Fe_3O_4 prepared using a conventional co-precipitation protocol.[52] With these assemblies of SD-MNPs a range of mean sizes from 5 to 14 nm is covered. These suspensions display distinctive interparticle interaction strengths and different degrees of MNP size polydispersity and aggregation. Although these colloids are not highly dissipative, they were selected because, with the exception of the uncoated MNPs, their blocking temperatures (for d.c. magnetometry measuring time $\tau_m \sim 100$ s) are below room temperature. In highly diluted colloids of single particles, the MNPs are almost non-interacting, constituting an easier study case but far from useful in a therapeutic scenario since by lowering the concentration larger amounts of suspension, beyond the tumour capacity, would have to be injected to achieve the desired temperature. Magnetocalorimetric measurement, and a.c. and d.c. magnetometry were used to determine the mean activation energy, and to confirm the presence of interparticle interactions. Transmission electron microscopy (TEM) and cryo-TEM were used to determine the mean nanoparticle size, the dispersity and the occurrence of aggregation. The so-derived physical properties were used to numerically simulate the SAR and to validate the extrapolation to other field conditions.

2. Experimental section

2.1 Synthesis of SD-IONP suspensions

In this work five colloidal aqueous suspensions are analysed. Two were obtained using the microwave (MW)-assisted thermal decomposition method at 180 °C and 210 °C followed by electrostatic stabilization with tri-sodium citrate (Na_3Cit). These samples consist of γ-Fe_2O_3 particles with a mean magnetic core size of 5.6 and 8.0 nm and are labelled as Cit/MNP-6 and Cit/MNP-8. The other two samples were produced by co-precipitation of iron(II) sulfate and iron(III) chloride hexahydrate with the addition of oleic acid (OA) to produce coated Fe_3O_4 nanoparticles followed by a second step where these particles were coated with chitosan (CS). The mean magnetic core sizes of these particles are 5 and 10 nm, and they are named here as CS/MNP-5 and CS/MNP-10. These material consist of large CS particles holding well-spaced MNP particles in the former case and quite aggregated particles in the latter. A deeper discussion on the synthesis protocol and physico-chemical characterization as well as magnetic characterization can be found elsewhere.[47,51] Finally, a colloid of uncoated magnetite, named U/MNP-14 here, was used. These particles with a mean size of around 14 nm were produced by co-precipitation of iron(III) chloride hexahydrate and iron(II) chloride tetrahydrate. Synthesis details and complete structural and magnetic characterization have

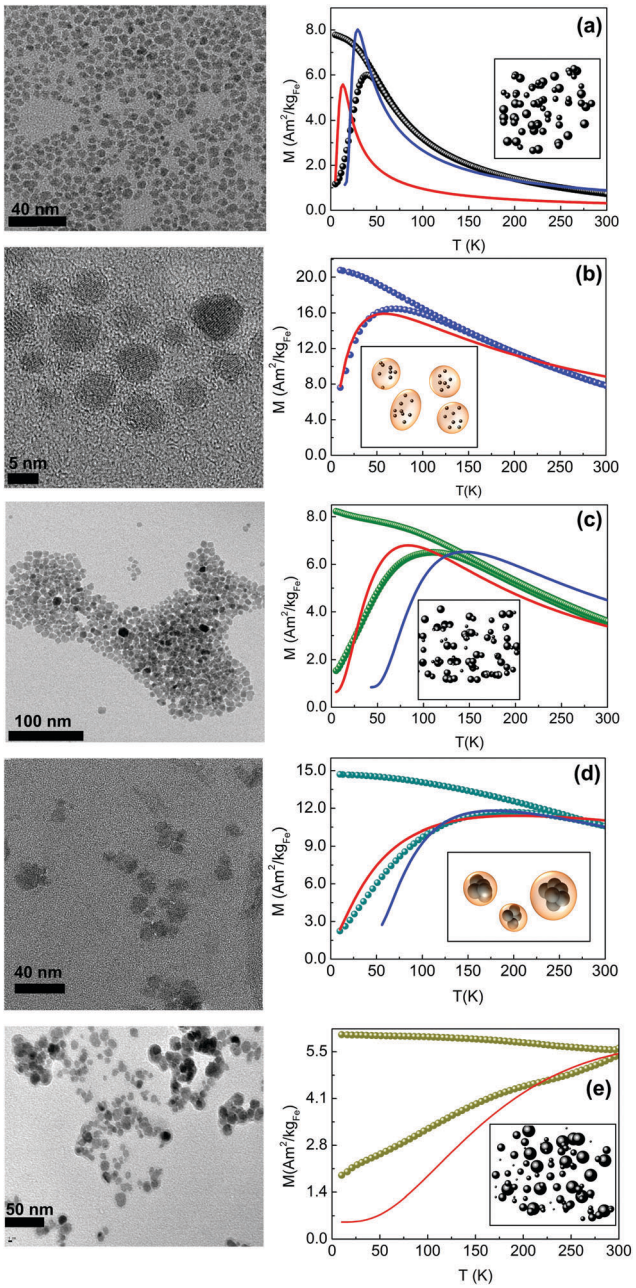

Fig. 1 Representative TEM images, and magnetization behavior under ZFC/FC protocols for (a) Cit/MNP-6, (b) CS/MNP-5, (c) Cit/MNP-8, (d) CS/MNP-10 and (e) U/MNP-14. Continuous lines correspond to ZFC magnetization simulations using the Tournus and Bonet model[63] (eqn (3)), red color considering size dispersity using the distribution function derived from TEM images, and blue color considering both size dispersity and dipolar interactions using the Vogel–Fulcher approximation. The cartoons on the right of the plots schematize nanoparticle structuring.

been previously published.[52] The main structural characteristics are schematized in Fig. 1. The MW-assisted thermal decomposition method was used to synthesize pristine SD-IONPs in a CEM Discover reactor (Explorer 12-Hybrid) at a frequency of 2.45 GHz and 300 W. The synthesis process is described in Yu *et al.*[53] following a slight modification from Pascu *et al.*[54] Briefly, 0.124 g (0.35 mmol) of tri-(acetylacetonate) iron(III) ($Fe(acac)_3$) was dissolved completely in 4.5 mL of anhydrous benzyl alcohol in a special MW-tube and vortexed for 30 seconds. Reaction tubes were transferred to the microwave reactor, the heating ramps were 5 min at 60 °C and 10 min at 180 °C or 10 min at 210 °C for the 5.6 and 8.0 nm particles respectively. Once the reaction finished, 150 μL of 10 wt% Na_3C was added to each MW-tube and sonicated for 1 min. Then, the suspension of SD-IONPs in each tube was divided into 2 equal parts in separate 50 mL centrifuge tubes. Each centrifuge tube was filled up to 50 mL with acetone and subjected to centrifugation at 6000 rpm for 30 min. The supernatant was discarded and the operation was repeated twice. SD-IONPs were washed and centrifuged again under the same conditions. The collected SD-IONP pellets were dried overnight in an oven at 60 °C and dispersed in 2 mL of MilliQ water. The colloidal concentration [X] was determined by flame atomic absorption spectroscopy using a Perkin-Elmer spectrometer. To obtain CS/MAG nanoparticles, 3.27 g of $FeCl_3{\cdot}6H_2O$ (12.1 mmol of Fe^{3+}) and 0.981 g of $FeSO_4$ (6.46×10^{-3} mol Fe^{2+}) were dissolved in 100 mL of distilled water and OA was incorporated into the mixture. Then, 25 ml of 5 M NaOH was added at a controlled rate to precipitate the oxide. The mixture was allowed to complete magnetite formation for 30 min. Washing cycles with bi-distilled water were carried out three times. The solid was dried at 45 °C overnight under vacuum. In the second step, 450 mg of CS was used to hydrophilize 300 mg of oleic-acid coated magnetite (OA/MAG) nanoparticles (2/3 of CS to OA/MAG w/w) previously synthesized with different mass ratios of oleic acid to magnetite (1/1 and 4/1). Around 300 mg of OA/MAG was dispersed in acetone under sonication for 15 min. Then, an adequate volume of a solution of 9.73 mg ml^{-1} of CS in acetic acid (50%) was incorporated. The solid nanoparticles were decanted immediately. The supernatant was removed and the solid was dispersed in distilled water.

For uncoated magnetite, 2.75 g of $FeCl_3{\cdot}6H_2O$ (10.2 mmol of Fe^{3+}) and 1.01 g of $FeCl_2{\cdot}4H_2O$ (5.1 mmol of Fe^{2+}) were each dissolved in 50 mL of bi-distilled water, mixed and heated to 60 °C. Then, 3 mL of NH_4OH solution (25% w/w) was added drop by drop and left to react for 30 min; after that, 75 mL of ammonia solution was added until the solution reached a pH of 10.5. Then, the black precipitate was separated from the dispersion medium, washed several times and re-suspended in water at pH = 7.

2.2 Structural and magnetic characterization

TEM micrographs and electron diffraction (ED) images were obtained using a JEOL JEM-1210 electron microscope, operating at 120 kV. The mean diameter and polydispersity of each system were determined by counting and sizing over 300 particles from TEM images using ImageJ software and fitting a Gaussian distribution to the resulting particle size histograms. Samples for cryo-transmission electron microscopy (cryo-TEM) were prepared as follows: 3 μL of 2.5 μg mL^{-1} IONPs was placed onto a Quantifoil® grid where a perforated foil was used to bear an ultra-thin carbon support foil to minimize the total specimen thickness. The drop was blotted with filter paper and the grid was quenched rapidly into liquid ethane to produce vitreous ice,

avoiding the formation of crystals. The grid was then transferred into the TEM microscope (JEM-2011 operating at 200 kV), where the temperature was kept at 133 K by the use of liquid nitrogen during the imaging.

The hydrodynamic sizes of the nanoparticles suspended in water were investigated with dynamic light scattering (DLS) using a Zetasizer Nano ZS from Malvern Instruments equipped with a He/Ne 633 nm laser. Care was taken that the DLS peak position and width were the same after three consecutive runs of 15 scans each run for all the nanoparticles. Number distribution data are reported.

Magnetic characterization was performed using a superconductive quantum interference device (SQUID) Quantum Design MPMS5XL magnetometer working in the temperature range of 5–400 K and in the magnetic field range of 0–5 T. Zero field cooled (ZFC) and field cooled (FC) experiments were carried out by measuring the static magnetization at a H_{DC} field of 50 Oe (4 kA m^{-1}) as the temperature was swept at a rate of 2 K min^{-1} from 5 to 300–400 K in samples cooled in the absence of an applied field, M_{ZFC}, and in samples cooled in a H_{DC} field, M_{FC}. Isothermal specific magnetization, M, loops under applied magnetic field, H, at various temperatures between 5 and 300 K with a maximum H of 5 T were performed for the ZFC samples. The a.c. susceptibility in the frequency range between 11 and 1000 Hz was obtained using a SQUID magnetometer and to enlarge the a.c. measurement frequency range the a.c. susceptibility option of Quantum Design PPMS 9T having a measuring range of up to 10 kHz was also used. To avoid nonlinear magnetization effects a low enough field amplitude $H_{a.c.}$ = 5 Oe (0.4 kA m^{-1}) was chosen. Data were acquired at various frequencies ($f = \omega/2\pi$) ranging from 11 to 9999 Hz. The temperature range 5–300 K was well below the ordering temperature (873 K, 858 K) of the magnetic phase (maghemite, magnetite). Therefore changes in saturation magnetization M_s are rather small, and so the temperature dependence of M_s is neglected for a.c. susceptibility data analysis.

The samples were prepared using gelatin capsules filled with compacted cotton impregnated with 50 μL of aqueous nanoparticle suspension giving a mass of around 1 mg of magnetic material, or just encapsulating the colloidal suspension into a heat shrinkable tube to prevent sample evaporation and spills. The specific magnetization values are reported per mass of iron.

Magnetocalorimetric experiments under radiofrequency fields for determining the SAR were conducted by exposing 0.5 mL of the aqueous suspensions, held in a clear glass Dewar, to a field of frequencies of 163, 171, 190, 230 and 260 kHz and amplitudes from 16 to 52 kA m^{-1}. The field generator consists of a Hüttinger resonant RLC circuit (2.5/300) holding refrigerated water and 6 turn coils of 2.5 cm diameter. Temperature was sensed during the experiment using an optical fibre sensor placed in the centre of the sample. The sensor was connected to a calibrated signal conditioner (Neoptix) with an accuracy of ±0.1 °C. Application of the RF field was interrupted to keep the colloid temperature below 30 °C in order to minimize solvent evaporation and prevent its destabilization. Measurements were done in triplicate; reported values are average and s.d.

The SAR values were calculated from the initial slope $\partial T/\partial t$ of the experimental heating curves as $\mathrm{SAR} = \frac{C}{[x]}\frac{\partial T}{\partial t}$ where C is the volumetric heat capacity of the solvent (4.18 J K^{-1} cm^{-3}). The SAR is reported here, as W per gram of Fe. The heating curves are straight lines as commonly observed.[46,47]

3. Specific absorption rate defining parameters

The specific heat released by a single domain MNP at a given field frequency f and amplitude H_0 depends on the magnetic relaxation mechanism achieved by the MNPs. Within a characteristic time the magnetic moment switches from one direction to the opposite *i.e.* the magnetization reverses in a coherent way due to Néel or Brown processes. Brown relaxation times depend on medium viscosity, η, and hydrodynamic volume, V_H, as $\tau_B = \frac{3\eta V_H}{k_B T}$. The Néel relaxation time for uniaxial anisotropy depends on the energy barrier, U, of a double-well potential and on the inverse attempt frequency $\tau_0 \sim 10^{-13}$–10^{-10} s[55] as $\tau_N = \tau_0 \exp(U/k_B T)$. Extending this expression to include the field amplitude dependence gives $\tau_{N,h} = \tau_0 \exp(U(1-h)^2/k_B T)$, where $h = H_0/H_k$, H_k being the anisotropy field.[56] The dynamics of the particle's dipole moment are governed by the effective relaxation time, τ, given by $\tau^{-1} = \tau_N{}^{-1} + \tau_B{}^{-1}$. For independent relaxation modes,[57] faster relaxation occurs. The Néel mechanism is inhibited ($\tau_N \gg \tau_B$) when the particles are large and/or have large magnetic anisotropy. Brown relaxation is inhibited ($\tau_N \ll \tau_B$) when the particles display a large hydrodynamic volume and also hindered when the particles get fixed to cell membranes in the case of specific targeting.[58]

The dissipation caused by these switching processes gives rise to a complex magnetic susceptibility. The imaginary part of the susceptibility, $\chi''(f)$, is proportional to the component of the magnetization that is induced out of phase with the excitation wave. This component is directly proportional to the specific rate of energy dissipation,[11] known as the SAR (specific absorption rate) parameter which is given within the lineal response approximation[59] and Stoner–Wohlfarth (SW) theory[60] by:

$$\mathrm{SAR} = \mu_0 \pi f H_0{}^2 \int \chi''(f,\tau) g(\tau) \mathrm{d}\tau \quad (1)$$

With

$$\chi''(f,\tau) = \frac{2\pi f \tau}{1 + (2\pi f \tau)^2} \chi_0 \quad (2)$$

where $g(\tau)$ is the relaxation time distribution due to the nanoparticle size distribution, aggregation and dipolar interactions. At low field amplitude, χ_0 can be approximated by the d.c. initial specific susceptibility[11] and modelled as $\chi_0 \cong \frac{\mu_0 \rho M_s{}^2 V}{3 k_B T}$.

In this way SAR values of MNP of a given chemical phase characterized by density ρ, at T, f and H_0 depends on the physical properties of the nanoparticles such as their shape and volume, V (or size D), their dispersion and magnetic properties, such as anisotropy and saturation magnetization, M_s, interparticle interactions (closely related to concentration), and the viscous and rheological properties of the environment. Eqn (1) indicates that the SAR of SD-MNP suspensions increases with increasing field amplitude as ${H_0}^2$, with increasing f in a more complex way through the $f\chi''(f)$ factor (eqn (2)), with increasing saturation magnetization as ${M_s}^2$ and with increasing V as the $V\chi''(\tau(V))$ factor given by eqn (2). These dependencies have been experimentally proved, as was briefly reviewed in the introduction.[16,43]

The particles studied here dissipate by the Néel relaxation mechanism. It will be shown in the next section that τ_N is 6 orders of magnitude smaller than τ_B. Then, we will focus on the analysis of τ_N for complex colloids. For non-interacting particles of uniaxial anisotropy, U is related to MNP volume V as $K_{eff}\langle V\rangle$, where K_{eff} is the effective anisotropy constant. Interparticle dipolar interaction increases the relaxation time and has been modelled by adding a term to the energy barrier as $U = K_{eff}V + E_{in}$, where E_{int} represents mean field derived dipolar interparticle interaction energy, or alternatively by decreasing thermal energy. The latter is known as the Vogel–Fulcher correction and is a well-known approximation to account for weakly interacting nanoparticles.[61] It is clearly seen that the linear relation between U and V does not hold anymore for dipolar interacting nanoparticles simply recalling that the dipolar interaction between two particles is proportional to the square root of the particle magnetic moment μ^2 ($M_s = \mu/V$). Also, K_{eff} contains crystallographic, shape and surface contributions, and on the nanoscale it is highly dependent on the nanoparticle size.[16]

4. Results and discussion

As mentioned, we selected as model systems five stable colloidal aqueous suspensions to be studied on the basis of their distinctive M_{ZFC} and M_{FC} temperature behavior shown in Fig. 1 (right), with the aim of analysing activation energy, anisotropy and the applicability of eqn (1) to semi-empirically predict their SAR magnitude from the knowledge of their physical properties. These colloids consist of SD-IONPs of uniaxial anisotropy axes distributed in random directions. The mean MNP sizes cover a range from 5 to 14 nm, and they differ in terms of nanoparticle size dispersity and structuring according to the TEM images shown in Fig. 1 (left). The Cit/MNP-6 (mean size 6 nm) and Cit/MNP-8 (mean size 8 nm) particles are highly monodisperse and display somehow faceted faces. The CS/MNP-10 colloid consists of CS particles (~49 nm size) containing aggregates of 10 nm size MNPs densely packed. The distance between the particles is close to the contact distance, thus dipolar interactions are strong. On the other hand, the CS/MNP-5 colloid consists of CS particles (~53 nm) containing well-spaced 5 nm size MNPs (almost no dipolar interactions are expected).[47] U/MNP-14 displays a larger polydispersity and a high degree of aggregation.[52] ED was carried out in all of the studied samples. ED images display well-defined diffraction rings that could be indexed to the cubic spinel structure (JCPDS#19-629) as exemplified in Fig. S1 of the ESI.† Also an XRD pattern and its refinement is shown in Fig. S1-c of the ESI†. The main structural data, mean size D and standard deviations (used here as a measurement of the polydispersity degree) were derived from the fitting of Gaussian distributions to size histograms built from TEM images (see Table 1 and Fig. S1 of the ESI†).

Regarding M_{ZFC} and M_{FC} temperature behaviour, the Cit/MNP-6 nanoparticle assembly displays a well defined narrow peak with a maximum at 38 K; above the irreversible temperature T_i both curves coincide indicating superparamagnetic behaviour, and this region is well fitted by a Curie law function. The M_{ZFC} of the CS/MNP-5 nanoparticle assembly peaks at 66 K, at a larger temperature than for Cit/MNP-6 although its size is smaller than that of Cit/MNP-6, due to larger size dispersity (see Table 1). The Cit/MNP-8 nanoparticle assembly shows a somehow broader peak with a maximum at 111 K, CS/MNP-10 at 193 K, and U/MNP-14 well above room temperature. $M_{ZFC}(T)$ behaviour above T_i deviates from the Curie law for all of these samples except for Cit/MNP-6. In Fig. 1 samples are ordered with increasing blocking temperature, which also means increasing SAR magnitude, from top to bottom. The ZFC-FC magnetization curves besides reflecting structural features mainly distinguish isolated particles from interactive particle behaviours. For example, FC curves (see Fig. 1) reach a plateau in contrast to the increasing behaviour expected for a random non-interacting particle system, pointing

Table 1 Synthesis conditions, and colloid and nanoparticle properties. [x] is the colloid concentration expressed as mg of iron per mL of water, D and s.d. are the mean MNP size and standard deviation determined from TEM histograms, D_H and $s.d_H$ are the hydrodynamic size and the standard deviation of number distribution function derived from DLS measurements, μ and M_s are the mean nanoparticle magnetic moment and the saturation magnetization derived from the fit of d.c. magnetic loops measured at 300 K (see Fig. S3 of the ESI) and the SAR is the specific absorption rate measured in the colloidal suspensions at a field frequency of 260 kHz and a field amplitude of 52 kA m^{-1}. Co-pre stands for co-precipitation and TD-MW for thermal decomposition assisted with microwaves

Sample	Synthesis protocol	[x] (mg_{Fe} mL^{-1})	D (nm)	s.d. (nm)	D_H (nm)	$s.d_H$ (nm)	μ (μ_B)	M_s (A m^2 kg_{Fe}^{-1})	SAR (W g_{Fe}^{-1})
CS/MNP-5	Co-pre	1.2 ± 0.1	4.8	2.1	134.6	7.7	4009 ± 8	73.2 ± 3.0	11 ± 4
Cit/MNP-6	TD-MW	9.5 ± 0.2	5.6	0.8	52.2	26.0	1763 ± 2	57.5 ± 2.9	9 ± 1
Cit/MNP-8	TD-MW	14.7 ± 0.3	8.0	2.0	17.2	4.8	7146 ± 17	71.9 ± 2.9	7 ± 1
CS/MNP-10	Co-pre	2.3 ± 0.1	9.7	4.5	56.9	7.7	8053 ± 36	63.4 ± 2.6	114 ± 1
U/MNP-14	Co-pre	6.0 ± 0.1	13.6	5.3	1500	500	13 480 ± 256	90.0 ± 3.6	352 ± 6

out a strong interaction between particles, more noticeable for the CS/MNP-10 and U/MNP-14 samples. The interparticle interaction is detected by the shift of blocking temperature to higher values.[62] In complex colloids, this shift is also altered by features arising from polydispersity.

To get a better understanding of the influence of the dipolar interaction, size dispersity and aggregation on the thermally activated magnetization behaviour, simulations of M_{ZFC} were carried out following the Tournus and Bonet model:[63]

$$M_{ZFC} = \int_0^{\infty} \left(\frac{\mu_o \mu(r)^2 H}{3K_{eff} V(r)} e^{-\nu \delta t} + \frac{\mu_o \mu(r)^2 H}{3k_B T} \left(1 - e^{-\nu \delta t}\right) \right) g(r) dr \quad (3)$$

where $\mu(r)$ is the magnetic moment of a nanoparticle of radius r, $\nu = 1/\tau$ where $\tau = \tau_0 \exp[K_{eff} V(r)/k_B(T - T_0)]$ is the Néel relaxation time including Vogel–Fulcher correction T_0, which will be retrieved below from a.c. data analysis, $\delta t = \frac{k_B(T - T_0)}{u K_{eff} V(r)}$ where u is the heating rate, and $g(r)$ is the radii distribution derived from TEM (parameters listed in Table 1) by fitting the histograms.

In Fig. 1 simulations carried out considering only size dispersity (null T_0) are shown as red lines and those considering both size dispersity and dipolar interactions (T_0 values listed Table 2) are shown as blue lines. In simulations at $T = T_0$ the relaxation time is ∞ and all of the particles are blocked. The simulations take into account the effects of size dispersity and dipolar interactions but somehow disregard the effect of aggregation. The latter has been only considered through dipolar interactions within the Vogel–Fulcher correction, which is a good approximation for weakly interacting nanoparticles. Clearly, interactions among particles inside an aggregate are expected to be strong. The simulations verify the fact that structuring, size dispersity and dipolar interactions play a relevant role in the switching behaviour and then in the nanoparticle dissipation properties for MH.

From these data a distribution of activation energies $f(U)$ was obtained[64] as $\frac{\partial(M_{FC} - M_{ZFC})}{\partial T} \propto f(T_B) = \frac{f(U)}{k_B \ln(\tau_m/\tau_0)}$, valid when H_{DC} (4 kA m^{-1}) is smaller than anisotropy field H_K. The H_K magnitudes derived from the 5 K magnetic loop (4000, 3197, 2798, 1040, 754 kA m^{-1} for samples listed in Table 1 from top to bottom) satisfy this condition. The results are shown in Fig. 2. Both data and simulations verify the fact that blocking temperature increases with MNP size, and its value shifts to higher values with increasing size dispersity and interaction strength.

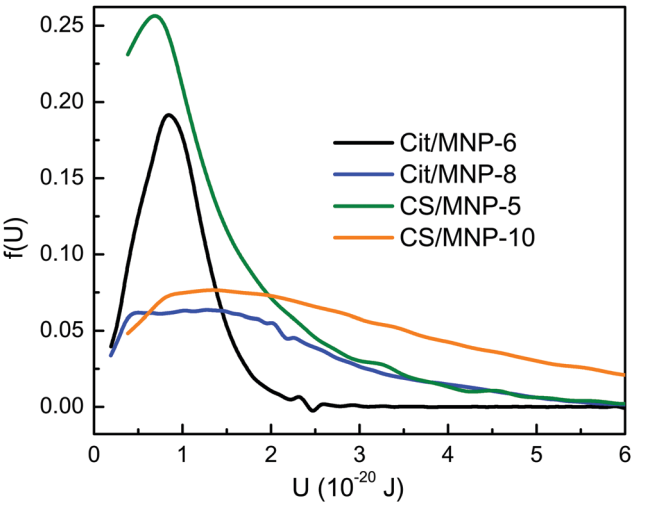

Fig. 2 Activation energy distribution derived from ZFC/FC data.

It can also be pointed out that ZFC/FC curves reflect magnetic anisotropic and dipolar interactions rather than Zeeman interactions because measurements are recorded at a low d.c field.

The precedent discussion proved that the idea of deriving K_{eff} from the blocking temperature $T_b = -U/(k_B \ln(\tau_0/\tau_m))$ using $\tau_m = 100$ s and $U = K_{eff} V + E_{int}$ and $V = \langle V \rangle$ derived from TEM may result in a K_{eff} value that is not accurate enough and fail to reproduce the SAR values. The studied colloids display three non-negligible characteristics: polydispersity, aggregation and dipolar interactions. Even Cit/MNP-6 and Cit/MNP-8 display size polydispersity and small aggregates as shown with cryo-TEM measurements (see Fig. 4). A colloid of nearly non-interacting MNPs can be obtained by lowering the concentration by dilution, but diluted colloids are far-away from the *in vivo* scenario[12] and even from the *in vitro* experiments where the MNPs are located in endosomes.[65] Also for low concentration a larger volume would have to be injected to achieve the therapeutic temperature, overcoming tumour capacity and the minimum non-toxic dosage. Cytotoxicity depends on size, shape, charge, surface area, and aggregation of IONPs. Generally, low or no cytotoxicity associated with the kind of IONPs studied here for exposure levels lower than 100 μg mL^{-1} was found.[66] The concentrations used here, listed in Table 1, are in the same order of magnitude as those used for *in vivo* experiments with mice tumour models.[67]

Table 2 Activation energy and specific absorption rate. U_{H_c}, U_{AC} and U_{SAR} are the mean activation energy values derived from coercive field temperature dependence, from a.c. susceptibility data analysis and from magnetocalorimetric measurements carried out at 260 kHz and 52 kA m^{-1}, respectively. μ_{H_c} is the mean magnetic moment derived from the $H_c(T)$ fit, n_p is the ratio $\frac{\mu_{H_c}}{\mu}$, T_0 is the Vogel-parameter and $\langle \tau_N \rangle$ is the mean relaxation time derived from SAR data analysis and τ_B is the Brown relaxation time

Sample	U_{H_c} (10^{-20} J)	μ_{H_c} (μ_B)	n_p	U_{AC} (10^{-20} J)	T_0 (K)	$\langle \tau_N \rangle$ (10^{-9} s)	τ_B (ms)	U_{SAR} (10^{-20} J)
CS/MNP-5	1.24 ± 0.08	32 827 ± 5137	8 ± 1	1.37 ± 0.14	0.01 ± 0.46	5.0 ± 0.9	0.70 ± 0.01	1.40 ± 0.08
Cit/MNP-6	0.74 ± 0.01	12 642 ± 364	7 ± 1	0.52 ± 0.06	13.45 ± 2.50	8.1 ± 0.8	0.04 ± 0.01	1.09 ± 0.04
Cit/MNP-8	1.09 ± 0.02	18 973 ± 656	3 ± 1	1.10 ± 0.13	38.69 ± 5.47	2.0 ± 0.3	0.0015 ± 0.0003	1.30 ± 0.06
CS/MNP-10	3.27 ± 0.08	65 961 ± 2901	8 ± 1	3.13 ± 0.48	47.43 ± 23.52	4.6 ± 0.1	0.06 ± 0.02	1.6 ± 0.01
U/MNP-14	6.2 ± 0.2	174 917 ± 9016	13 ± 1	—	—	344 ± 4	1030 ± 38	7.19 ± 0.01

Also, there is usually not enough knowledge about either the proportion of these three effects, or the correlation among them, or on how the relaxation time is modified by them. As a simple solution to this, we have derived the mean activation energy $\langle U \rangle$, which includes modifications of the energy barrier coming from the three mentioned effects. Values of $\langle U \rangle$ were consistently derived from independent measurements of a.c. susceptibility, coercive field, H_c, temperature dependence in the blocked range, as follows from the d.c. hysteresis loops, ZFC/FC protocols and magnetocalorimetric measurements under RF fields. The $\langle U \rangle$ values found in this work are consistent with energy barrier values reported in the literature for similar size iron oxide nanoparticles[20,28,52,68,69] as shown in Fig. S2 in the ESI.† The qualitative shape of the activation energy distribution derived from ZFC/FC magnetization measurements is shown in Fig. 2. For all of the analysis τ_0 was fixed at 10^{-10} s. This time value was chosen from the detailed analysis of Dormann *et al.*[61] who demonstrated, using a wide experimental measuring time range going from 10^{-8} to 10^{-1} s, that for interacting nanoparticles the dependence of $\log(\tau)$ against $(1/T_b)$ deviates from the Néel-Arrhenius law and asymptotically goes to $\tau_0 = 10^{-10}$ s.

A.C. susceptibility measurements exhibited the typical expected behaviour for SD-MNPs[61] (Fig. S4 of the ESI†). A well-defined maximum appears in the out-of-phase $\chi''(T)$ susceptibility at T_b. The peak positions shift with increasing frequency to higher values. Also the $\chi''(T)$ peak becomes broader, and shifts towards higher temperatures for increasing size dispersity, aggregation and interaction strength. Then, the Vogel–Fulcher criterion[70] was used to take into account these changes and to quantify interparticle interactions as $\ln\left(\frac{1}{2\pi f}\right) = \frac{U}{T_b - T_0} + \ln(\tau_0)$ where f is the excitation field frequency and T_0 is a parameter that globally accounts for interparticle interactions. Results are shown in Fig. 3a and U and T_0 fitted values are listed in Table 2.

The H_c of an assembly of randomly oriented single-domain MNPs exhibiting thermally activated coherent magnetization reversal follows, according to SW theory, the relation[71]

$$H_c(T) = 0.96\frac{K_{eff}}{\mu_0 M_s}\left[1 - \left(\frac{T}{T_b}\right)^{1/2}\right] = 0.96\frac{U}{\mu_0 \mu}\left[1 - \left(\frac{k_B T \ln(\tau_m/\tau_0)}{U + k_B T_0 \ln(\tau_m/\tau_0)}\right)^{1/2}\right] \quad (4)$$

where in the right part of eqn (4) the Volgel–Fulcher approximation for the relaxation time is included.

Fig. 3b depicts the dependence of H_c against $(T/T_b)^{1/2}$. The larger the blocking temperature the smaller the slope of $H_c(T)$, and the larger the SAR. Data were fitted using μ and U as fitting parameters (see Table 2) instead of K_{eff} and T_b as is often found in the literature. The so-derived U values are in good agreement with those obtained from $\chi''(T)$ analysis. The fitted μ values are listed as μ_{H_c} in Table 2 and are larger than μ of a SD-MNP (listed in Table 1) reflecting aggregation. The radio values $\frac{\mu_{H_c}}{\mu} = n_p$ are listed in Table 2.

Aggregation can also be inferred from DLS; the hydrodynamic sizes are listed in Table 1. The colloids CS/MNP-5 and CS/MNP-10 are composed of polymeric particles holding well-spaced MNPs or their aggregates as can be seen using TEM as was previously shown using SAXS.[47] For U/MNP-14 colloids, prepared with uncoated MNPs, aggregation occurs on many length scales, as is deduced from the large D_H value and also seen in the TEM images. On the other hand, aggregation is not so clear in the TEM images of Cit/MNP-6 and Cit/MNP-8 nanoparticles. Then, cryo-TEM was used to verify the presence of aggregates in these colloids. When the particles are prepared for cryo-TEM the cooling is so fast that the solvent freezes but the particle positions remain unchanged. In the images shown

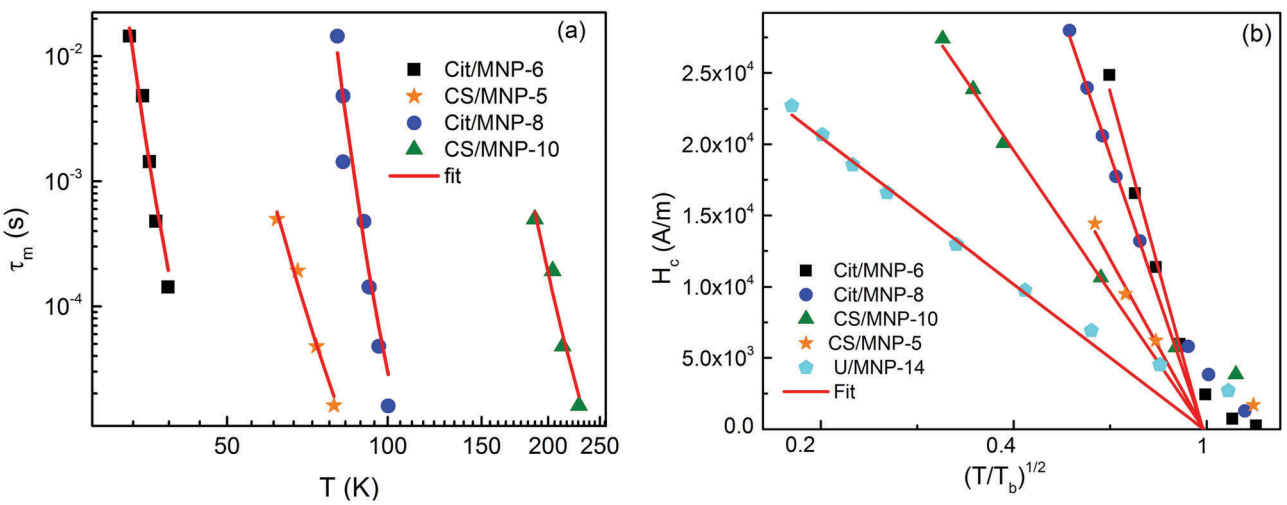

Fig. 3 (a) Measuring time τ_m of a.c. susceptibility measurements *vs.* temperature T. Continuous lines represent the best fits obtained using the Vogel–Fulcher model. (b) Coercive field H_c temperature dependence derived from d.c. magnetization curves. T_b is the blocking temperature for SQUID measuring time τ_m = 100 s and $\tau_0 = 10^{-10}$ s. Continuous lines represent the best fits obtained using eqn (4). From these fits the mean energy barrier U_{H_c} and mean magnetic moment μ_{H_c} are obtained.

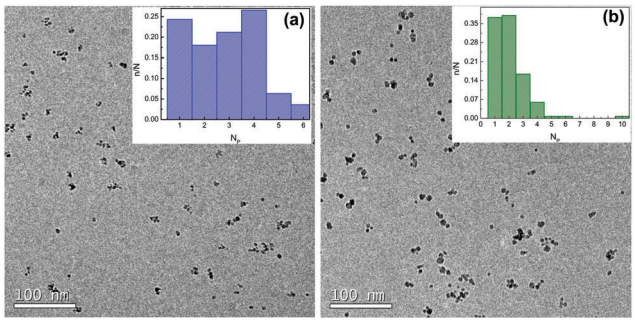

Fig. 4 Cryo-TEM images of (a) Cit/MNP-6 and (b) Cit/MNP-8 samples. Inset: n/N is the frequency count of the number of aggregates n containing N_p particles, N being the total number of aggregates.

in Fig. 4, single particles and aggregates of only a few particles can be observed. Chain like arrangements appear consistent with the minimum energy configuration of the dipole–dipole interactions (head–tail). The frequency n/N of the number of aggregates n containing N_p particles, N being the total number of aggregates, was derived from the images and is shown in the inset of Fig. 4. A large fraction of the particles are composed of small aggregates, 85% for Cit/MNP-6 and 75% for Cit/MNP-8.

The previous analysis has shown that real colloids useful for biomedical applications, to a greater or lesser degree, always display size dispersity, aggregation and non-negligible interaction among particles, and these facts occur in both colloids designed to display isolated particles and those designed to contain multicores.

The particles studied here dissipate by the Néel relaxation mechanism; the Brown relaxation times estimated using water viscosity $\eta = 0.7978 \times 10^{-3}$ Pa s and the hydrodynamic sizes listed in Table 1 consistently result in relaxation times much larger than τ_N listed in Table 2.

Next, we analyse the heating curves measured while the colloids were exposed to an excitation field of 260 kHz and 52 kA m^{-1} (raw data are shown in Fig. S5 of the ESI†). From the SAR data combined with the physical properties listed in Table 1 we have extracted a mean $\langle \tau_{N,h} \rangle$ value so that values obtained with eqn (1) reproduce the experimental SAR values under the applied field conditions. For this analysis we used the Néel relaxation time as $\tau_{N,h}$, with h calculated using the anisotropy field derived from 5 K magnetization curves. In this way, it was possible to retrieve a mean activation energy value (listed in Table 2 as U_{sar}) from the relaxation time (SAR measurements). It can be seen that there is good agreement between the independently derived U values. Notice that low frequency a.c. measurements and d.c. magnetometry were carried out in frozen samples and the switching corresponds to the Néel mechanism. The good agreement between these U values and those derived from magnetocalorimetric measurements in the colloids confirms that the Brown mechanism is inhibited in our colloids. Large differences appear for Cit/MNP-6.

We selected the Cit/MNP-6 colloid, due to the large disagreement between the different U measurements, and the CS/MNP-10 colloid, due to its higher SAR magnitude under our larger available f and H_0 conditions, to examine frequency and field amplitude dependence. To this end, heating curves were recorded at various field amplitudes at a fixed frequency (see Fig. 5a) and at various field frequencies holding a constant field amplitude (see Fig. 5b). The SAR linearly increases with H_0^2 and with f as predicted with eqn (1), as expected within the linear response theory. Then, the so-derived relaxation time was used to extrapolate, using eqn (1), the SAR to the other frequencies and field amplitudes (red lines in Fig. 5a and b). It can be seen that the extrapolated values provide a good approximation to SAR values measured in these ranges of frequencies and amplitudes. Importantly, we have shown that the most significant physical property to be determined for predicting the heating efficiency of a given colloid is the distribution of the activation energy or the energy barrier. The latter contains contributions from anisotropy, dipolar interaction strength

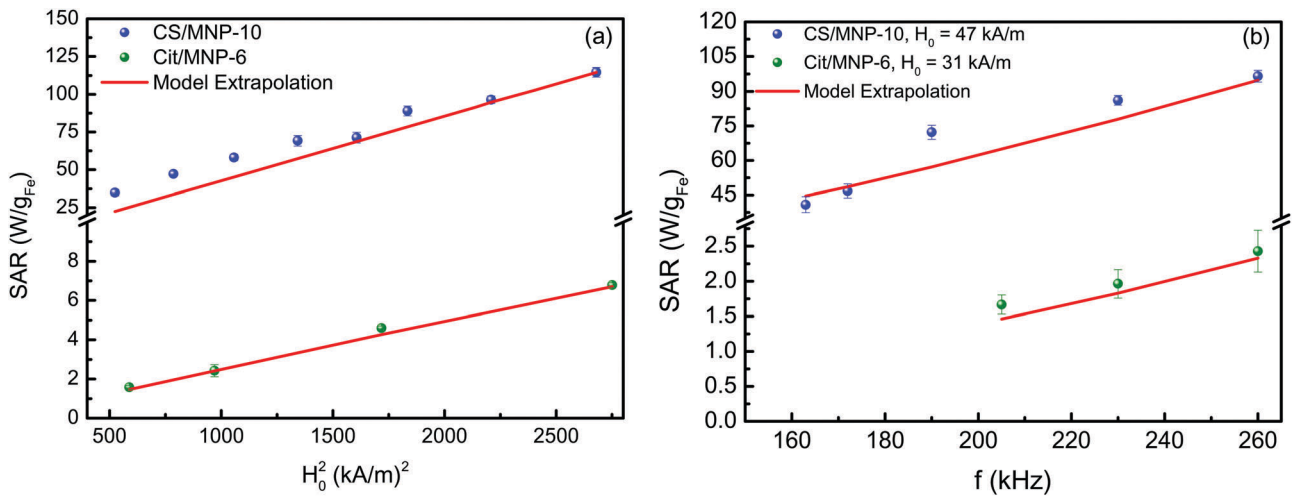

Fig. 5 For samples CS/MNP-10 and Cit/MNP-6: (a) specific absorption rate (SAR) *vs.* square field amplitude H_0. (b) SAR *vs.* field frequency f. Continuous lines represent the extrapolation to different field conditions of eqn (1) using the relaxation time retrieved from static and dynamic measurements.

among particles and aggregation. As these features often appear in an uncontrolled manner, the specific proportion of the contribution of each property is disregarded, but the so-derived global mean activation energy includes all the mentioned contributions. We hitherto conclude that the physical properties of a colloidal dispersion that must be determined to securely predict its heating efficiency at any pre-set applied field using the analytical expression (eqn (1)) are mean activation energy, nanoparticle saturation magnetization and MNP volume distribution. We believe that our findings may assist medical decisions serving at least as a guide for a better choice of optimal nanoparticle dosage, or at fixed dosage, better selection of clinical conditions. Overall, clinical settings, f and H_0, jointly with MNP heating efficiency determine the dosage. In the first view, heating efficiency at a given field is determined by K, V, and M_s. However, concentration and aggregation play a crucial role modifying the energy barrier. The SAR concentration dependence is non-monotonous,[31,39] because the long range nature of dipolar interaction and aggregation may decrease heating efficiency when the magnetic moments are randomly oriented inside the aggregates,[30–33] but the formation of elongated chains may improve it.[27,34] Also aggregate compactness plays a role. In loose aggregates the SAR decrease remained moderate, this decrease being much larger for more compact packing.[32] These results stress the fact that magnetic hyperthermia prediction is a quite complex problem and the use of just K, V, and M_s is not enough for determining nanoparticle heating efficiency. Our solution differs from other previously proposed approaches by characterizing the material type with $\langle U \rangle$, $\langle V \rangle$ and M_s, where U includes the other effects besides anisotropy terms (KV). A different promising strategy has been proposed by Ruggiero *et al.*[14] The authors analysed oleate-covered iron oxide nanoparticles incorporated into poly(lactic-*co*-glycolic acid) particles and showed that ^{1}H nuclear magnetic relaxation dispersion profiles (as measured at very low magnetic fields, 0.01 MHz) can be correlated with the SAR of the system when exposed to an alternating magnetic field of 177 kHz and 18 kA m^{-1}.

The complexity of magnetic hyperthermia prediction increases in *in vitro* experiments with MNP aggregates inside endosomes, where the number of filled endosomes and their sizes vary from cell to cell, and the compactness of the MNPs inside the endosomes depends on the type of cell and on the IONP size distribution and surface charge. Less dense endosomes were observed for anionic magnetite nanoparticles compared with the uncoated nanoparticles.[65] Even a more complex scenario appears in *in vivo* experiments where after intratumoral infiltration irregular distribution patterns of the magnetic materials occur due to high interstitial pressures at the tumour area.[15] Although good results have been obtained pre clinically with animals, the control of the intratumoral distribution of the MNPs is an unsolved problem. It is clear that heating efficiency changes when going from suspension to cell cultures or to tumours. Nevertheless, finding a way to predict the SAR under various field conditions is a hurdle that needs to be overcome. Such knowledge together with controlled tumour distribution patterns will be useful to predict the heat distribution in tumours.

4. Conclusions

We have addressed the issue of predicting the heating efficiency of real biomedical colloids for magnetic hyperthermic therapy. Real magnetic colloids are very complex systems because they display size dispersity, aggregation and their concentration must be in the useful range, where dipolar interactions are relevant. Comparing the activation energy distribution, which defines Néel relaxation times, determined in four independent experiments, we can safely conclude that by knowing the mean nanoparticle volume, its saturation magnetization and a representative mean activation energy, the specific absorption rates can be predicted under a given field condition. This knowledge may assist the medical decision on the optimal nanoparticle dosage considering tumour volume and the desired temperature increase.

Abbreviations

CA	Citric acid
DLS	Dynamic light scattering
FC	Field cooling
ICP-AES	Atomic emission spectroscopy with induced plasma Coupled
IONPs	Iron oxide nanoparticles
MNPs	Magnetic nanoparticles
RF	Radio frequency
SAR	Specific absorption rate
SD	Single domain
SQUID	Superconducting quantum interference device
TEM	Transmission electron microscopy
ZFC	Zero field cooling

Author contributions

The manuscript was written through contributions of all authors. All authors have given approval to the final version of the manuscript.

Acknowledgements

This research was funded by CONICET (PIP 0720) and UNLP-X11/680 grants of Argentina and also partially funded by the Spanish Ministry of Economy (MAT2015-64442-R andSEV-2015-0496 projects, co-funded with European Social Funds) and the Generalitat de Catalunya (2014SGR213). We thank V. Lassalle for providing multicore nanoparticles, E. de Sousa for synthesizing uncoated nanoparticles and D. Muraca for TEM data acquisition at Brazilian Nanotechnology National Laboratory (LNNano), Centro Nacional de Pesquisa em Energia e Materiais (CNPEM), Brazil under the Project No. TEM-MSC-14825.

References

1 K. Maier-Hauff, F. Ulrich, D. Nestler, H. Niehoff, P. Wust, B. Thiesen, H. Orawa, V. Budach and A. Jordan, *J. Neuro-Oncol.*, 2011, **103**, 317.

2 Y. Ren, H. Zhang, B. Chen, J. Cheng, X. Cai, R. Liu, G. Xia, W. Wu, S. Wang, J. Ding, C. Gao, J. Wang, W. Bao, L. Wang, L. Tian, H. Song and X. Wang, *Int. J. Nanomed.*, 2012, **7**, 2261.
3 K. Sub Kim, J. Kim, J. Young Lee, S. Matsuda, S. Hideshima, Y. Mori, T. Osaka and K. Na, *Nanoscale*, 2016, **8**, 11625.
4 A. Ruiz, P. C. Morais, R. B. de Azevedo, G. M. Lacava, A. Villanueva and M. del Puerto Morales, *J. Nanopart. Res.*, 2016, **16**, 2589.
5 M. Dan, Y. Bae, T. A. Pittman and R. A. Yokel, *Pharm. Res.*, 2014, **32**(5), 1615.
6 Y. Zhai, H. Xie and H. Gu, *Int. J. Hyperthermia*, 2015, **25**(1), 65.
7 I. Rabias, D. Tsitrouli and E. Karakosta, *Biomicrofluidics*, 2009, **4**(2), 024111.
8 A. Jordan, R. Scholz, K. Maier-Hauff, F. K. van Landeghem, N. Waldoefner, U. Teichgraeber, J. Pinkernelle, H. Bruhn, F. Neumann, B. Thiesen, A. von Deimling and R. Felix, *J. Neuro-Oncol.*, 2006, **78**(1), 7.
9 P. Moroz, S. K. Jones and B. N. Gray, *J. Surg. Oncol.*, 2001, **77**, 259.
10 S. Luo, L. F. Wang, W. J. Ding, H. Wang, J. M. Zhou, H. K. Jin, S. F. Su and O. A. Ouyang, *Cancer*, 2014, **2**(1), 2.
11 R. E. Rosensweig, *J. Magn. Magn. Mater.*, 2002, **252**, 370.
12 A. Jordan, R. Scholz, P. Wust, H. Fähling and R. Felix, *J. Magn. Magn. Mater.*, 1999, **201**, 413.
13 J. Grossman and S. E. McNeil, *Phys. Today*, 2012, **65**(8), 38.
14 M. R. Ruggiero, S. G. Crich, E. Sieni, P. Sgarbossa, M. Forzan, E. Cavallari, R. Stefania, F. Dughiero and S. Aime, *Nanotechnology*, 2016, **27**, 285104.
15 I. Hilger, *Int. J. Hyperthermia*, 2013, **29**(8), 828.
16 I. M. Obaidat, B. Issa and Y. Haik, *Nanomaterials*, 2015, **5**, 63.
17 P. de la Presa, Y. Luengo, M. Multigner, R. Costo, M. P. Morales, G. Rivero and A. Hernando, *J. Phys. Chem. C*, 2012, **116**(48), 25602.
18 R. Hergt, S. Dutz, R. Müller and M. Zeisberger, *J. Phys.: Condens. Matter*, 2006, **18**, 2919.
19 S. Sun, H. Zeng, D. B. Robinson, S. Raoux, P. M. Rice, S. X. Wang and G. Li, *J. Am. Chem. Soc.*, 2004, **126**, 273.
20 G. Salas, C. Casado, F. J. Teran, R. Miranda, C. J. Serna and M. Puerto Morales, *J. Mater. Chem.*, 2012, **22**, 21065.
21 P. Hugounenq, M. Levy, D. Alloyeau, L. Lartigue, E. Dubois, V. Cabuil, C. Ricolleau, S. Roux, C. Wilhelm, F. Gazeau and R. Bazzi, *J. Phys. Chem. C*, 2012, **116**(29), 15702.
22 J. P. Novoselova, A. P. Safronov, O. M. Samatov, I. V. Beketov, H. Khurshid, Z. Nemati, H. Srikanth, T. P. Denisova, R. Andrade and G. V. Kurlyandskaya, *IEEE Trans. Magn.*, 2014, **50**(11), 4600504.
23 L. Gonzalez-Moragas, S. M. Yu, N. Murillo-Cremaes, A. Laromaine and A. Roig, *Chem. Eng. J.*, 2015, **281**, 87.
24 C. Blanco-Andujar, D. Ortega, P. Southern, Q. A. Pankhurst and N. T. Thanh, *Nanoscale*, 2015, **7**(5), 1768.
25 E. Alphandéry, *Front Bioeng. Biotechnol.*, 2014, **2**, 5.
26 M. Marciello, V. Connord, S. Veintemillas-Verdaguer, M. A. Vergés, J. Carrey, M. Respaud, C. J. Serna and M. Puerto Morales, *J. Mater. Chem. B*, 2013, **1**, 5995.
27 C. Martinez-Boubeta, K. Simeonidis, A. Makridis, M. Angelakeris, O. Iglesias, P. Guardia, A. Cabot, L. L. Yedra, S. Estrade, F. Peiro, Z. Saghi, P. A. Midgley, I. Conde-Leboran, D. Serantes and D. Baldomir, *Sci. Rep.*, 2013, **3**, 1652.
28 R. Di Corato, A. Espinosa, L. Lartigue, M. Tharaud, S. Chat, T. Pellegrino, C. Ménager, F. Gazeau and C. Wilhelm, *Biomaterials*, 2014, **35**, 6400.
29 J. H. Lee, J. T. Jang, J. S. Choi, S. H. Moon, S. H. Noh, J. G. Kim, J. G. Kim, I. S. Kim, K. I. Park and J. Cheon, *Nat. Nanotechnol.*, 2011, **6**, 418.
30 J. G. Ovejero, D. Cabrera, J. Carrey, T. Valdivielso, G. Salas and F. J. Teran, *Phys. Chem. Chem. Phys.*, 2016, **18**, 10954.
31 D. F. Coral, P. Mendoza Zélis, M. Marciello, M. del Puerto Morales, A. Craievich, F. Sanchez and M. Fernández van Raap, *Langmuir*, 2016, **32**(5), 1201.
32 C. Guibert, V. Dupuis, V. Peyre and J. Fresnais, *J. Phys. Chem. C*, 2015, **119**(50), 28148.
33 M. E. Materia, P. Guardia, A. Sathya, M. Pernia Leal, R. Marotta, R. Di Corato and T. Pellegrino, *Langmuir*, 2015, **31**(2), 808.
34 D. Serantes, K. Simeonidis, M. Angelakeris, O. Chubykalo-Fesenko, M. Marciello, M. del Puerto Morales, D. Baldomir and C. Martinez-Boubeta, *J. Phys. Chem. C*, 2014, **118**, 5927.
35 M. Jeun, S. Bae, A. Tomitaka, Y. Takemura, K. Ho Park, S. Ha Paek and K. W. Chung, *Appl. Phys. Lett.*, 2009, **95**, 082501.
36 A. Urtizberea, E. Natividad, A. Arizaga, M. Castro and A. Mediano, *J. Phys. Chem. C*, 2010, **114**(11), 4916.
37 D. Serantes, D. Baldomir, C. Martinez-Boubeta, K. Simeonidis, M. Angelakeris, E. Natividad, M. Castro, A. Mediano, D. X. Chen, A. Sanchez, L. I. Balcells and B. Martínez, *J. Appl. Phys.*, 2010, **108**, 073918.
38 B. Mehdaoui, R. P. Tan, A. Meffre, J. Carrey, S. Lachaize, B. Chaudret and M. Respaud, *Phys. Rev. B: Condens. Matter Mater. Phys.*, 2013, **87**, 174419.
39 I. Conde-Leboran, D. Baldomir, C. Martinez-Boubeta, O. Chubykalo-Fesenko, M. P. Morales, G. Salas, D. Cabrera, J. Camarero, F. Teran and D. Serantes, *J. Phys. Chem. C*, 2015, **119**(27), 15698.
40 G. T. Landi, *Phys. Rev. B: Condens. Matter Mater. Phys.*, 2014, **89**, 014403.
41 G. T. Landi, *J. Appl. Phys.*, 2013, **113**, 163908.
42 C. Haase and U. Nowak, *Phys. Rev. B: Condens. Matter Mater. Phys.*, 2012, **85**, 045435.
43 E. C. Abenojar, S. Wickramasinghe, J. Bas-Concepcion and A. C. S. Samia, *Prog. Nat. Sci.: Mater. Int.*, 2016, **26**, 440.
44 G. Salas, J. Camarero, D. Cabrera, H. Takacs, M. Varela, R. Ludwig, H. Dähring, I. Hilger, R. Miranda, M. del Puerto Morales and F. J. Teran, *J. Phys. Chem. C*, 2014, **118**(34), 19985.
45 D. Kechrakos and K. N. Trohidou, *Appl. Phys. Lett.*, 2002, **81**, 4574.
46 P. Mendoza Zélis, G. A. Pasquevich, S. J. Stewart, M. B. Fernández van Raap, J. Aphesteguy, I. J. Bruvera, C. Laborde, B. Pianciola, S. Jacobo and F. H. Sánchez, *J. Phys. D: Appl. Phys.*, 2013, **46**, 125006.
47 D. F. Coral, P. Mendoza Zelis, M. E. de Sousa, D. Muraca, V. Lassalle, P. Nicolas, M. L. Ferreira and M. B. Fernández van Raap, *J. Appl. Phys.*, 2014, **115**, 043907.

48 E. Lima Jr, T. E. Torres, L. M. Rossi, H. R. Rechenberg, T. S. Berquo, A. Ibarra, C. Marquina, M. R. Ibarra and G. F. Goya, *J. Nanopart. Res.*, 2013, **15**, 1654.

49 M. S. Carrião and A. F. Bakuzis, *Nanoscale*, 2016, **8**, 8363.

50 J. M. Orozco-Henao, D. F. Coral, D. Muraca, O. Moscoso-Londoño, P. Mendoza Zélis, M. B. Fernández van Raap, S. K. Sharma, K. R. Pirota and M. Knobel, *J. Phys. Chem. C*, 2016, **120**(23), 12796.

51 P. Nicolás, M. Saleta, H. Troiani, R. Zysler, V. Lassalle and M. L. Ferreira, *Acta Biomater.*, 2013, **9**(1), 4754.

52 M. E. de Sousa, M. B. Fernández van Raap, P. C. Rivas, P. Mendoza Zélis, P. Girardin, G. Pasquevich, J. Alessandrini, D. Muraca and F. H. Sánchez, *J. Phys. Chem. C*, 2013, **117**(10), 5436.

53 S. Yu, A. Laromaine and A. Roig, *J. Nanopart. Res.*, 2014, **16**, 2484.

54 O. Pascu, E. Carenza, M. Gich, S. Estradé, F. Peiró, G. Herranz and A. Roig, *J. Phys. Chem. C*, 2012, **116**(28), 15108.

55 J. L. Dormann, L. Bessais and D. Fiorani, *J. Phys. C: Solid State Phys.*, 1988, **21**, 2015.

56 J. Dieckhoff, D. Eberbeck, M. Schilling and F. Ludwig, *J. Appl. Phys.*, 2016, **119**, 043903.

57 M. I. Shliomis and V. I. Stepanov, *Advances in Chemical Physics: Relaxation Phenomena in Condensed Matter*, John Wiley & Sons, 1994.

58 F. Sonvico, S. Mornet, S. Vasseur, C. Dubernet, D. Jaillard, J. Degrouard, J. Hoebeke, E. Duguet, P. Colombo and P. Couvreur, *Bioconjugate Chem.*, 2005, **16**, 1181.

59 J. Jensen and A. R. Mackintosh, *Rare Earth Magnetism: Structures and Excitations*, Oxford, 1991.

60 E. C. Stoner and E. P. Wohlfarth, *Philos. Trans. R. Soc., A*, 1948, **240**, 599.

61 J. L. Dormann, D. Fiorani and E. Tronc, *Magnetic relaxation in fine particle systems: in Advances in Chemical Physics*, John Wiley & Sons, 2007.

62 J. M. Vargas, W. C. Nunes, L. M. Socolovsky, M. Knobel and D. Zanchet, *Phys. Rev. B: Condens. Matter Mater. Phys.*, 2005, **72**, 184428.

63 F. Tournus and E. Bonet, *J. Magn. Magn. Mater.*, 2011, **323**, 1109.

64 F. Luis, J. M. Torres, L. M. García, J. Bartolomé, J. Stankiewicz, F. Petroff, F. Fettar, J.-L. Maurice and A. Vaurés, *Phys. Rev. B: Condens. Matter Mater. Phys.*, 2002, **65**, 094409.

65 M. Elisa de Sousa, A. Carrea, P. Mendoza Zélis, D. Muraca, O. Mykhaylyk, Y. E. Sosa, R. G. Goya, F. H. Sánchez, R. A. Dewey and M. B. Fernández van Raap, *J. Phys. Chem. C*, 2016, **120**(13), 7339.

66 U. S. Patil, S. Adireddy, A. Jaiswal, S. Mandava, B. R. Lee and D. B. Chrisey, *Int. J. Mol. Sci.*, 2015, **16**(10), 24417.

67 S. Kossatz, R. Ludwig, H. Dähring, V. Ettelt, G. Rimkus, M. Marciello, G. Salas, V. Patel, F. J. Teran and I. Hilger, *Pharm. Res.*, 2014, **31**, 3274.

68 V. Dolgovskiy, V. Lebedev, S. Colombo, A. Weis, B. Michen, L. Ackermann-Hirschi and A. Petri-Fink, *J. Magn. Magn. Mater.*, 2015, **379**, 137.

69 G. Vallejo-Fernandez, O. Whear, A. G. Roca, S. Hussain, J. Timmis, V. Pattel and K. O'Grady, *J. Phys. D: Appl. Phys.*, 2013, **46**, 312001.

70 J. L. Dormann, L. Spinu, E. Tronc, J. P. Jolivet, F. Lucari, F. D. D'Orazio and D. Fiorani, *J. Magn. Magn. Mater.*, 1998, **183**, 255.

71 H. Pfeiffer, *Phys. Status Solidi A*, 1990, **119**, 295.